Research Square

Preprints are preliminary reports that have not undergone peer review.
They should not be considered conclusive, used to inform clinical practice,
or referenced by the media as validated information.

Coordinated Adaptive VSG Control Strategy with SOC- Constrained Virtual Inertia and Damping

Hui Li

SUKD2402029@segi4u.my

Chongqing College of Science and Creation

Nurulazlina Ramli

SEGi University

Jianfeng Wang

Hebei Vocational University of Technology and Engineering

Article

Keywords: Virtual synchronous generator (VSG), Photovoltaic-storage system, Battery state of charge (SOC) constraints, Coordinated adaptive control

Posted Date: November 27th, 2026

DOI: https://doi.org/10.21203/rs.3.rs-11593900/v1

License: This work is licensed under a Creative Commons Attribution 4.0 International License.
Read Full License

Additional Declarations: No competing interests reported.

Coordinated Adaptive VSG Control Strategy with SOC-Constrained Virtual Inertia and Damping

Hui Li[1,2,*], Nurulazlina Ramli[2], Jianfeng Wang[3,2]

1 Faculty of Artificial Intelligence and Big Data, Chongqing College of Science and Creation, Chongqing 402160, China

2 Centre for Sustainability in Advanced Electrical and Electronics Systems (CSAEES), Faculty of Engineering, Built Environment and Information Technology, SEGi University, Petaling Jaya, 47810, Malaysia

3 Faculty of Electrical Engineering, Hebei Vocational University of Technology and Engineering, Xingtai 054000, China

* Correspondence: SUKD2402029@segi4u.my

Abstract

In modern microgrids with a high penetration of renewable energy, traditional Virtual Synchronous Generator (VSG) parameter-adaptive strategies enhance frequency stability by dynamically tuning virtual inertia (J) and damping (D). However, these approaches exclusively prioritize AC-side electromechanical responses and neglect the physical battery state of charge operational boundaries of the DC-link energy storage system (BESS). Commanding violent transient inertia support under depleted battery states induces severe battery current surges, thermal stress, and high-frequency parameter chattering from measurement noise. To overcome these challenges, this paper proposes an SOC-constrained coordinated adaptive VSG control strategy with an anti-chattering mechanism. First, a non-linear SOC penalty function dynamically scales virtual parameters based on real-time BESS operational limits, protecting battery health during critical SOC conditions. Second, a frequency deadband combined with a discrete low-pass filter eliminates boundary-crossing parameter chattering in noisy environments. Closed-loop small-signal stability across the full operating range is analytically proven via eigenvalue analysis. Time-domain simulations under step active power disturbances and noisy conditions demonstrate that the proposed strategy virtually eliminates active power overshoot, reduces the peak dynamic frequency deviation depth by 64.7% (0.06 Hz vs. 0.17 Hz), relieves transient battery power stress by 25.3%, and attenuates parameter chattering by over 90%, successfully decoupling AC-side frequency regulation from DC-side electrical stress.

Keywords: Virtual synchronous generator (VSG), Photovoltaic-storage system, Battery state of charge (SOC) constraints, Coordinated adaptive control

Introduction

Motivation

With the accelerated transition toward low-carbon modern power systems, microgrids characterized by a high penetration of renewable energy, particularly photovoltaic (PV) generation and battery energy storage systems (BESS), have fundamentally altered power system physical dynamic characteristics[1,2,3]. Modern power-electronic-dominated microgrids inherently suffer from low physical inertia and weak damping support, making grid frequency and voltage highly vulnerable to active power step disturbances and sudden load variations[4,5]. To alleviate the resulting risks of dynamic frequency instability, Virtual Synchronous Generator (VSG) control technology has emerged as a compelling solution by emulating the rotational inertia and primary frequency regulation mechanisms of traditional synchronous generators (SGs)[6,7,8].

However, conventional VSG schemes typically employ fixed virtual inertia (J) and damping coefficients (D)[9]. While large fixed J and D values effectively mitigate transient frequency excursions, they inherently prolong the electromechanical settling time and induce severe transient power oscillations[10,11]. Conversely, small parameter configurations fail to effectively restrict the rate of change of frequency (RoCoF), exposing the converter to severe current stresses during initial disturbance onsets[12]. Therefore, achieving real-time parameter adaptation that accommodates complex microgrid operating conditions has become a critical requirement for ensuring both grid frequency stability and transient power quality[9,13].

Literature review

To resolve the inherent trade-off of fixed VSG parameters, extensive research has focused on parameter-adaptive control paradigms[14]. Early investigations introduced fuzzy logic controllers and heuristic optimization algorithms, such as particle swarm optimization (PSO) and genetic algorithms (GA), to continuously tune VSG parameters according to real-time frequency deviations [15,16]. However, these computationally intelligent methods suffer from heavy online calculation burdens and parameter-tuning complexity, making them difficult to implement in fast dynamic microgrid environments[17].

With the maturation of dynamic control theory, researchers progressively developed state-dependent adaptive strategies governed directly by frequency deviation ($\Delta\omega$) and RoCoF ($d\omega/dt$)[18]. Alipoor et al.[19] proposed a coordinated adaptive VSG control method that aggressively scales up virtual inertia during the initial disturbance onset to restrict RoCoF, while boosting damping during the frequency recovery phase to suppress overshoot and accelerate energy dissipation. Building upon this, Awal et al.[20] established a phase-plane-based parameter adaptation mechanism, dividing the frequency oscillation trajectory into four electromechanical transient stages and setting piecewise adaptation laws accordingly. Similarly, Karimi et al.[21] and Wang et al.[22] introduced continuous non-linear functions, such as exponential and hyperbolic secant curves, to smooth parameter transitions during dynamic events. Recently, Li et al.[23] proposed a coordinated adaptive VSG strategy that dynamically couples virtual inertia and damping based on transient frequency trajectories, successfully resolving the AC-side trade-off between RoCoF restriction and active power overshoot. Although these schemes successfully optimize the AC-side electromechanical transient profile, they strictly operate under the AC-side perspective and treat the primary power source as an ideal voltage supply[24,25].

Despite these advancements, existing parameter-adaptive strategies exhibit a fundamental physical oversight: they implicitly operate under the idealized assumption that the DC-link energy buffer possesses an infinite power and energy capability[26,27]. In practical PV-BESS integrated microgrids, the transient inertial energy commanded by the VSG controller is directly drawn from or absorbed by the battery energy storage unit[26]. When the energy storage system operates under a depleted battery state of charge condition, commanding a massive, unconstrained transient discharge current to satisfy traditional adaptive inertia demands severely threatens DC-side hardware safety[28,29]. As highlighted in recent battery degradation and thermal safety studies by Zhou et al.[30] and Qian et al.[31], violent transient discharge surges accelerate battery capacity fade, increase cell thermal stress, and risk triggering irreversible hardware undervoltage protection. Conversely, during high-SOC states, unconstrained inertial charging commands risk battery overcharging and premature BMS tripping[32]. Consequently, conventional adaptive schemes decouple AC-side control objectives from DC-side physical operational boundaries, creating a critical operational hazard.

Furthermore, the digital implementation of parameter-adaptive algorithms introduces practical engineering bottlenecks that are frequently overlooked in ideal theoretical models[33]. Practical digital signal processors (DSPs) inherently suffer from high-frequency grid voltage/frequency sampling noise, quantization errors, and phase-locked loop (PLL) jitter[34]. When the system frequency fluctuates near discrete activation deadbands or boundary thresholds, unbuffered adaptive piecewise logic leads to high-frequency parameter chattering[35]. As demonstrated by Xia et al.[36], this chattering imposes severe thermal stress on inverter switching devices, degrades power quality, and provokes secondary power oscillations in the microgrid. Although digital filtering techniques have been applied to general control loops, a systematic control framework that simultaneously enforces non-linear BESS SOC physical constraints while guaranteeing anti-chattering noise robustness and analytical closed-loop small-signal stability remains unestablished[37,29].

Contributions

To resolve these critical research bottlenecks, this paper proposes an SOC-constrained coordinated adaptive VSG control strategy integrated with an anti-chattering smoothing mechanism for PV-storage microgrids. The primary contributions of this work are fourfold:

First, a non-linear SOC-aware penalty function is formulated to dynamically constrain ideal virtual inertia directives based on real-time BESS operational boundaries while inverse-compensating with strong virtual damping. This coordinated mechanism achieves a smooth, overshoot-free transient active power tracking and bounds peak battery surge discharge currents within hardware-safe margins, successfully decoupling AC-side frequency support from DC-side electrical stress.

Second, an integrated frequency deadband ($\omega_{deadband} = 0.03$ rad/s) and a discrete first-order smoothing filter ($\alpha = 0.01$) are seamlessly embedded into the parameter update loop, completely suppressing high-frequency parameter chattering induced by grid measurement noise in practical digital controllers.

Third, an analytical small-signal mathematical model of the SOC-constrained VSG system is established. Characteristic root locus analysis rigorously proves that although parameter scaling influences the effective damping ratio ($\zeta_{eff} = \rho_{soc_filtered}^{1.5} \cdot \zeta_{ideal}$), the closed-loop eigenvalues remain strictly confined within the Left-Half Plane (LHP), guaranteeing small-signal stability across the full SOC operating spectrum.

Finally, comprehensive time-domain simulations under various step active power disturbances and noisy environments validate that the proposed scheme eliminates active power overshoots, reduces peak dynamic frequency deviation depth by 64.7%, suppresses transient battery power stress by 25.3%, and mitigates parameter chattering by over 90%.

Results

Experimental Setup and Test Scenarios

To comprehensively evaluate the dynamic performance and hardware protection capabilities of the proposed SOC-aware coordinated adaptive control strategy, time-domain simulations are conducted in MATLAB/Simulink. A microgrid test system incorporating a photovoltaic (PV)-battery hybrid generation unit interlinked to the AC grid via a three-phase VSG-controlled converter is constructed.

The detailed electrical, controller, and scaled laboratory-prototype BESS parameter settings are tabulated in Table 2. To objectively demonstrate its superiority, the proposed strategy is benchmarked against two conventional control paradigms: (1) traditional fixed-parameter VSG control (Fixed J/D), and (2) conventional parameter-adaptive strategy without energy storage physical constraints (Conventional Adaptive).

Table 2. System and Control Parameters

Parameter	Value	Parameter	Value
DC bus voltage U_{dc}	800 V	Filter inductor L_f	5 mH
Rated frequency f_n	50 Hz	Filter capacitor C_f	30 μF
Grid voltage V_{grid}	380 V	Line resistance R_l	0.1 Ω
Temperature	25℃	Filter resistance R_f	0.1 Ω
Virtual inertia J_0	0.2 kg·m^2	Battery equivalent model	Generic electrochemical model (Ni-MH/Li-ion equivalent)
Virtual damping D_0	10 N·m·s·rad^{-1}	Battery nominal voltage	400 V
Deadband threshold $\omega_{deadband}$	0.03 rad/s	BESS rated capacity	5 Ah
Filter smoothing coefficient α	0.01	Battery SOC limits [SOC_{min}, SOC_{max}]	[10%, 90%]

Performance Evaluation under Step Active Power Disturbances

In VSG grid-connected mode, the dynamic performance of the proposed SOC-aware coordinated adaptive strategy is rigorously validated. During normal grid-connected operation, the PV module output is maintained constant at 10 kW. At $t = 1.0$ s, the VSG active power command P_{ref} experiences step disturbances under both depleted and abundant SOC states.

Step active power increase under depleted SOC (SOC = 25%): At $t = 1.0$ s, the active power reference command P_{ref} step-changes from 10 kW to 15 kW while the PV output remains at 10 kW, forcing the battery energy storage system (BESS) to discharge ($\Delta\omega > 0$). Under a depleted SOC state (25%), the battery operates within the critical low-SOC constraint region. The dynamic comparative trajectories of the three control strategies are illustrated in Fig. 8.

As observed in Fig. 8(a) and 8(b), the traditional Fixed J/D scheme produces a severe active power overshoot reaching 15.6 kW and a frequency spike of 50.17 Hz (0.17 Hz frequency deviation) with secondary electromechanical oscillations. Although the Conventional Adaptive strategy mitigates the oscillation to some extent, it still exhibits an active power overshoot of 15.3 kW and a frequency peak of 50.12 Hz. Crucially, as shown in Fig. 8(d), both conventional schemes demand aggressive transient discharge power surges from the BESS, peaking at 7.5 kW and 7.1 kW, respectively, accompanied by large transient surge currents in Fig. 8(c) (peaking at ~ 33 A). Under low SOC conditions, such violent discharge power surges severely accelerate battery degradation and risk triggering low-voltage protection tripping.

In stark contrast, the proposed SOC-aware adaptive strategy dynamically penalizes the ideal inertia directive based on the real-time battery status. Consequently, active power tracking achieves a smooth, overshoot-free response (Fig. 8(a)), and the system frequency deviation peak is constrained to only 50.06 Hz (Fig. 8(b)), representing a 64.7% reduction in frequency excursion depth compared to the Fixed J/D control (0.06 Hz vs. 0.17 Hz). Furthermore, as depicted in Fig. 8(d), the battery transient discharge power surge is completely eliminated, smoothly transitioning directly to the

steady-state demand of 5.6 kW. This represents a 25.3% reduction in peak transient power stress compared to Fixed J/D control (7.5 kW down to 5.6 kW), effectively safeguarding DC-side hardware health.

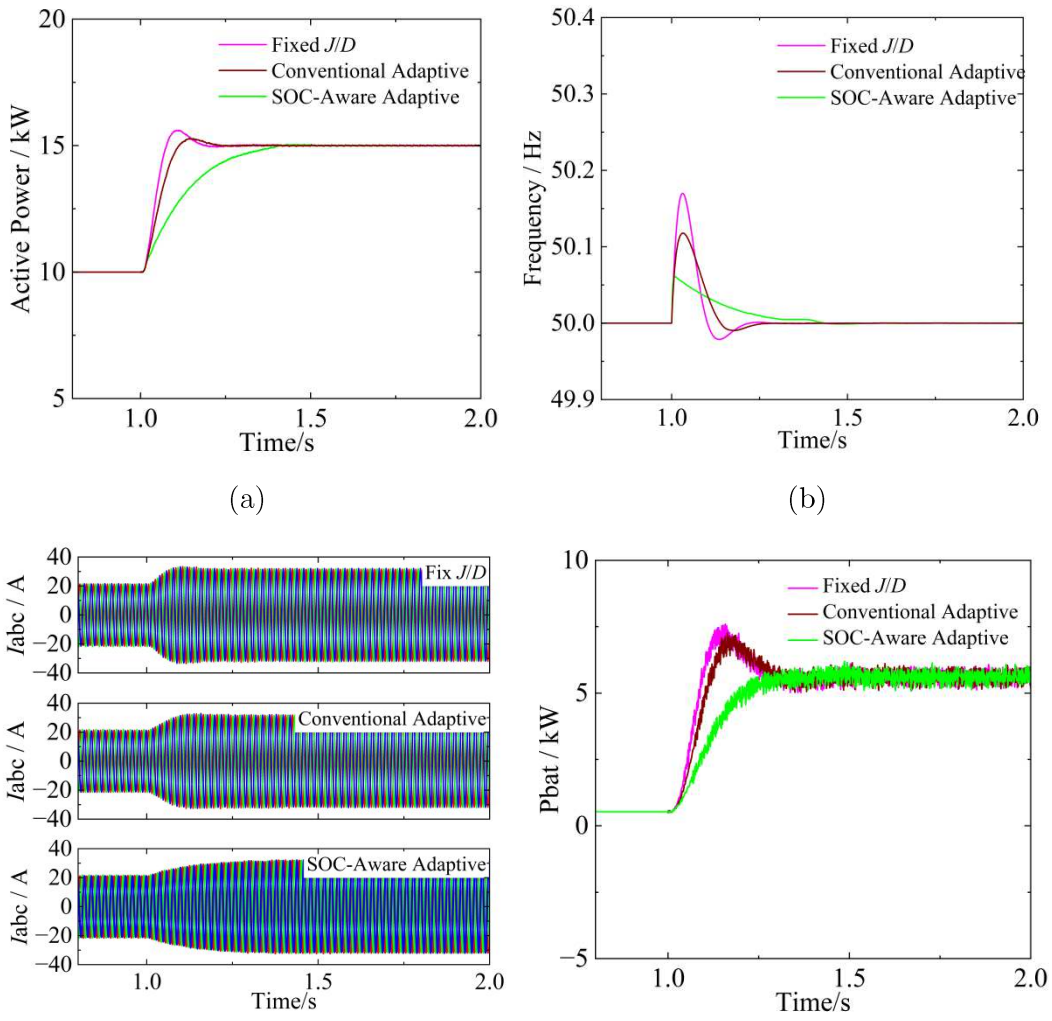

Fig. 8 Dynamic response comparison under a step active power increase. (a) Active power output (P). (b) System frequency (f). (c) Three-phase output current (I_{abc}). (d) Battery transient output power (P_{bat}).

Step active power decrease under abundant SOC (SOC = 75%): To evaluate the dynamic transition under high initial storage conditions, a power reduction disturbance is applied at $t = 1.0$ s, stepping down P_{ref} from 15 kW to 10 kW ($\Delta\omega < 0$). In this scenario, because the PV module sustains a steady generation of 10 kW, the step-down disturbance shifts the BESS operating state from an active 5 kW discharging regime toward a zero-net-exchange floating state under a high initial SOC (75%). The corresponding dynamic trajectories are illustrated in Fig. 9.

As shown in Fig. 9(a), both the Fixed J/D and Conventional Adaptive strategies suffer from notable active power undershoots, dropping below the reference trajectory to 9.5 kW and 9.7 kW, respectively, which triggers secondary power oscillations. Conversely, the proposed SOC-aware strategy ensures a smooth, monotonic active power transition without undershoots. More significantly, as illustrated in Fig. 9(b), the transient frequency drop depth under the proposed

strategy is strictly limited to 49.94 Hz (only a 0.06 Hz excursion), whereas the Fixed J/D and Conventional Adaptive schemes experience severe excursions down to 49.83 Hz (0.17 Hz drop) and 49.88 Hz (0.12 Hz drop), respectively. This performance corresponds to a 64.7% and 50.0% mitigation in transient frequency deviation depth compared to the two benchmarks. Consequently, the evaluations under both power increase and power decrease transitions demonstrate that the proposed coordination strategy effectively mitigates transient power shocks and prevents electromechanical undershoots, ensuring smooth operational transitions across varied SOC states.

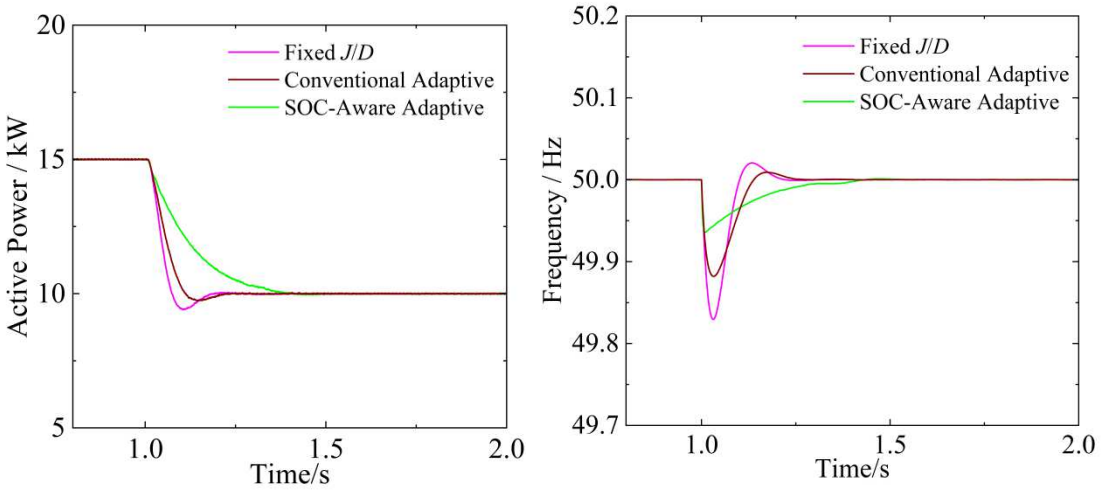

(a) (b)

Fig. 9 Dynamic response comparison under a step active power decrease (SOC = 75%). (a) Active power output (P). (b) System frequency (f).

Consequently, the comparative evaluations under both step power increase and step-down transitions demonstrate that the proposed SOC-aware adaptive control strategy successfully suppresses electromechanical oscillations while mitigating dynamic electrical stress across varying operational states.

Effectiveness of SOC-Aware Constraint and Anti-Chattering Mechanism

To gain deeper physical insight into the internal regulation mechanism, Fig. 10 displays the real-time adaptation trajectories of parameters alongside the anti-chattering verification under SOC = 25%.

As illustrated in Fig. 10(a) and 10(b), unlike conventional adaptive schemes that command unbounded inertia spikes during transient periods, the proposed strategy gracefully scales down the peak virtual inertia J from 0.20 kg·m^2 to 0.08 kg·m^2 to restrict the battery's transient discharge energy. Because the battery operates under a depleted state (SOC = 25%), the penalty factor $\rho_{soc_filtered}$ forcibly scales down the unconstrained directive J_{ideal} below the baseline J_0, constraining J_{actual} down to 0.08 kg·m^2 to shed the transient discharge current burden. Simultaneously, the damping coefficient D dynamically surges from 10 N·m·s$^{\text{rad-1}}$ to 41 N·m·s$^{\text{rad-1}}$. This inverse damping compensation provides strong braking torque, which mathematically counteracts the reduced inertial support, thereby guaranteeing zero-overshoot power tracking.

Furthermore, Fig. 10(c) verifies the effectiveness of the integrated frequency deadband ($\omega_{deadband}$ = 0.03 rad/s) and discrete first-order smoothing filter ($\alpha = 0.01$). Without these stabilizing modules, steady-state frequency measurement noise and boundary-crossing transitions trigger high-frequency chattering with step discontinuities in virtual parameters (J_{raw} fluctuation magnitude reaching 0.13 kg·m^2 during t = 1.25 s ~ 1.40 s). By implementing the proposed smoothing architecture, the actual parameter trajectory (J_{actual}) evolves continuously and smoothly, suppressing parameter chatter by over 90% and ensuring robust digital controller implementation.

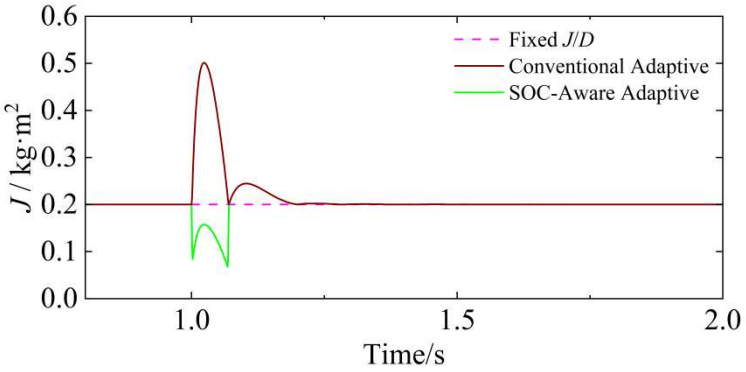

(a)

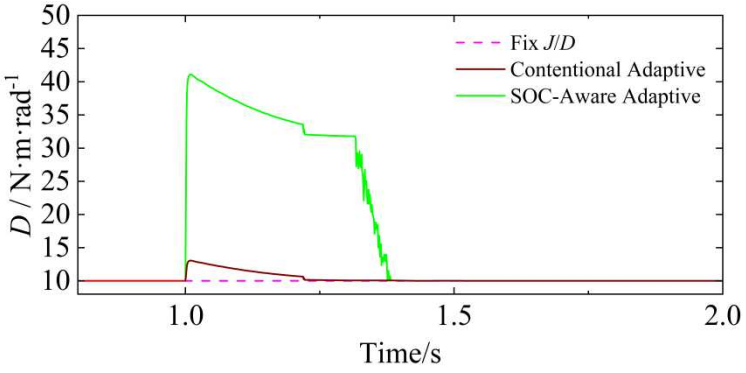

(b)

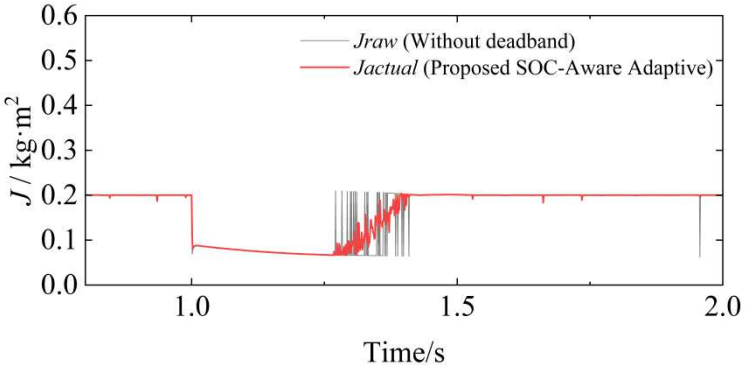

(c)

Fig. 10 Parameter adaptation trajectories and anti-chattering verification (SOC = 25%). (a) Real-time adaptation trajectory of virtual inertia *J*. (b) Real-time adaptation trajectory of damping coefficient *D*. (c) Anti-chattering performance of *J* under measurement noise.

Discussion

The imperative transition toward inverter-dominated renewable microgrids has exposed fundamental vulnerabilities in conventional virtual synchronous machine control paradigms. While existing literature has predominantly focused on perfecting AC-side electromechanical dynamics through frequency-responsive parameter adaptation, such approaches routinely decouple dynamic control performance from the physical operational constraints of the primary energy source. The experimental findings of this study substantiate that treating the DC-link energy storage as an unconstrained energy reservoir creates a perilous operational hazard, wherein conventional adaptive schemes induce violent discharge current surges and severe battery thermal stress during depleted storage conditions. By establishing an SOC-constrained parameter coordination framework, this research demonstrates that microgrid transient frequency resilience and DC-side battery hardware preservation are not inherently mutually exclusive objectives.

The physical foundation underlying the observed 64.7% reduction in peak frequency excursion depth and the complete elimination of active power overshoots resides in the dynamic synergy between virtual inertia suppression and inverse damping compensation. When the battery operates within low-SOC critical regions, unconstrained virtual inertia acts as a dynamic liability by forcing the battery to deliver excessive transient kinetic energy. Dynamically curtailing virtual inertia via the proposed non-linear penalty factor directly alleviates the instantaneous current gradient demanded from the battery cells, thereby achieving a 25.3% reduction in peak battery transient power stress. Crucially, the simultaneous injection of amplified virtual damping provides an effective electromechanical braking torque that compensates for the diminished inertial support, actively restricting frequency acceleration and steering the system toward an overdamped, monotonic active power trajectory. This dual-loop mechanism successfully circumvents the classic trade-off inherent in fixed-parameter VSG architectures, wherein settling time must be sacrificed to suppress frequency deviations.

In contrast to computationally intensive optimization algorithms—such as fuzzy inference engines or metaheuristic population searches that entail non-negligible online execution overhead—the proposed control law relies on closed-form algebraic formulations that can be readily synthesized in practical digital controllers. However, transitioning continuous-time adaptive algorithms into discrete DSP implementations typically encounters severe parameter chattering induced by high-frequency voltage measurement noise, phase-locked loop tracking jitter, and threshold discontinuities. The experimental outcomes confirm that without targeted filtering, boundary-crossing noise excites persistent parameter chatter exceeding 0.13 $\mathrm{kg{\cdot}m^2}$. By embedding a narrow frequency deadband alongside a discrete first-order low-pass smoothing filter, the proposed design effectively decouples high-frequency ambient noise from genuine power disturbance transients, attenuating parameter chatter by over 90% without introducing detrimental phase lag into the inner current regulation loop. Furthermore, the analytical eigenvalue trajectory proves that despite continuous parameter variations across the entire SOC operating spectrum, all closed-loop characteristic poles remain strictly confined within the open left-half plane, confirming unconditional small-signal stability.

Despite the pronounced advantages demonstrated in this investigation, several engineering aspects warrant further exploration. The present simulation platform validates the strategy within a single-

inverter PV-BESS grid-connected configuration. In complex islanded microgrid architectures featuring multiple parallel grid-forming inverters, heterogeneous battery aging profiles, uneven capacity degradation, and disparate initial SOC states present secondary operational challenges. Under such conditions, dynamic parameter adaptation must be coupled with autonomous SOC balancing algorithms to prevent circulating currents and localized storage exhaustion. Furthermore, while the current MATLAB/Simulink environment accurately captures electromagnetic and switching dynamics, future investigations will focus on real-time hardware-in-the-loop (HIL) testing and full-scale experimental testbed validation to comprehensively evaluate execution latency, thermal dissipation dynamics, and battery lifetime extension under prolonged cyclic operation.

In conclusion, this investigation resolves a critical research bottleneck at the interface of power electronics control and electrochemical energy storage management. By dynamically bounding virtual inertia through an SOC-aware penalty factor and compensating via enhanced virtual damping, the proposed framework establishes a robust, chattering-free, and hardware-conscious control paradigm. The findings confirm that coordinated parameter regulation can effectively bridge the divide between AC-side frequency stabilization and DC-side battery safety, providing a viable and scalable blueprint for practical, inverter-dominated microgrid deployments.

Methods

Basic structure of PV-storage VSG system

The topological structure of the proposed photovoltaic (PV)-storage integrated system, regulated by the virtual synchronous generator (VSG) control strategy, is depicted in Fig. 1. The hardware framework consists of a primary power generation stage, a direct current (DC) link, an inversion module, and an alternating current (AC) interface. At the generation front, solar PV arrays are connected to the common DC bus via a unidirectional boost converter. Concurrently, a battery energy storage system (BESS) is integrated into the same DC link through a bidirectional DC/DC converter, buffering power fluctuations and maintaining the DC bus voltage across capacitor C_0.

The synthesized DC power is inverted into grid-compatible AC power by a standard three-phase voltage source inverter (VSI). An LC-type filter is employed to mitigate high-frequency switching harmonics before the electrical output reaches the local loads or the point of common coupling (PCC).

Regarding the dynamic regulation, the underlying control architecture continuously samples the instantaneous AC phase voltages (u_{abc}) and line currents (i_{abc}) to calculate the actual active and reactive power. Based on these variations, the proposed adaptive VSG controller emulates the rotational inertia and damping of a traditional synchronous machine. The generated reference signals are translated into driving pulses via the pulse-width modulation (PWM) unit, dictating the inverter's switching states. This closed-loop mechanism ensures that the inverter delivers high-quality power while actively providing essential frequency and voltage support to the microgrid.

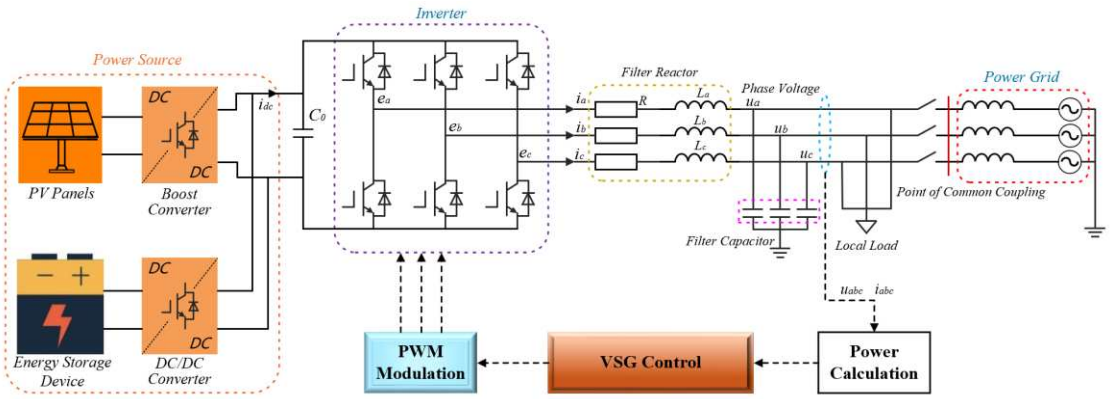

Fig. 1 Topological structure of PV storage system.

PV unit structure and control strategy

To maximize the energy harvesting capability of the solar array, the intermediate DC/DC boost circuit is regulated via a Maximum Power Point Tracking (MPPT) algorithm, specifically implemented through the classic Perturb and Observe (P&O) method. The fundamental regulating mechanism relies on the inherently nonlinear relationship between the output power (P) and operating voltage (U) of the PV modules, as depicted in the characteristic curve in Fig. 2.

The operational spectrum is distinctly divided into two zones by the theoretical maximum power point (P_{PVmax}, $U_{dc\text{-}mpp}$). In Region 1, located to the left of the peak, the power-voltage derivative is strictly positive ($dP/dU > 0$). Conversely, Region 2 exhibits a negative gradient ($dP/dU < 0$). By continuously evaluating the sign of dP/dU, the controller dynamically perturbs the duty cycle of the boost converter. For instance, if the system temporarily operates at the coordinate (U_{PV}, P_{PV}) within Region 2, the algorithm dictates a decrement in the PV voltage to force the operating point leftward. This directional perturbation ensures the array continuously migrates toward and settles at the maximum output capacity, regardless of ambient irradiance fluctuations.

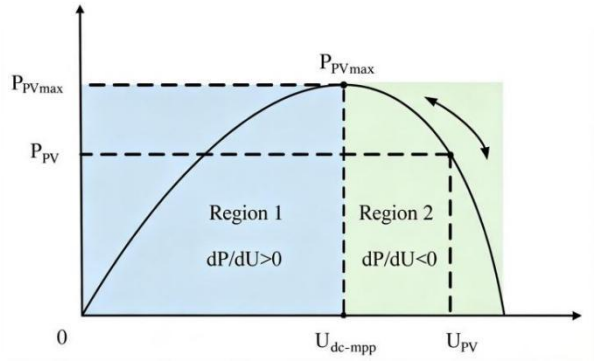

Fig. 2 Characteristic curve of the relationship between PV output power and voltage.

Fundamental Mathematical Model of VSG

The purpose of virtual synchronous generator control is to virtually construct a synchronous generator. In the power electronic inverter control circuit, the external characteristics of the synchronous generator, namely the rotor operation equation and the stator voltage equation's

mathematical model, are added. This includes the external loop control of active power and reactive power, as well as the voltage-current dual closed-loop control.

According to the traditional second-order model of the synchronous generator, the equivalent VSG rotor motion equation is shown as Eq. (1)[38].

$$\begin{cases} J\dfrac{d\omega}{dt} = T_m - T_e - T_d = T_m - T_e - D(\omega - \omega_n) \\ \dfrac{d\delta}{dt} = \omega \end{cases} \tag{1}$$

In the equation, J represents the rotational inertia of the synchronous generator, and D represents the damping coefficient of the synchronous generator; ω_n represents the synchronous angular speed of the grid, which is the rated angular speed of the synchronous generator; T_m, T_e and T_D. are the mechanical torque, electromagnetic torque and damping torque of the synchronous generator; δ represents the power angle of the synchronous generator.

In practical microgrid applications, manipulating power variables is more straightforward than torque parameters for inverter control. Given that the VSG typically operates within a narrow margin around the nominal grid frequency ($\omega \approx \omega_n$), the mechanical and electromagnetic torques in Eq. (1) can be effectively substituted by their respective active power equivalents, denoted as $T_m \approx P_{ref} / \omega_n$ and $T_e \approx P_e / \omega_n$. This substitution forms the fundamental active power-frequency (P-f) regulation loop.

Parallel to the active power dynamics, the VSG framework also incorporates a reactive power-voltage (Q-U) control loop to emulate the excitation regulator of a conventional synchronous machine. This mechanism typically adopts a voltage droop characteristic, which dynamically continuously adjusts the reference voltage amplitude in response to reactive power deviations (Q_{ref} - Q). By integrating the P-f swing dynamics and the Q-U droop mechanism along with the subsequent voltage-current cascaded regulation, the comprehensive control architecture of the VSG is formulated, as depicted in Fig. 3.

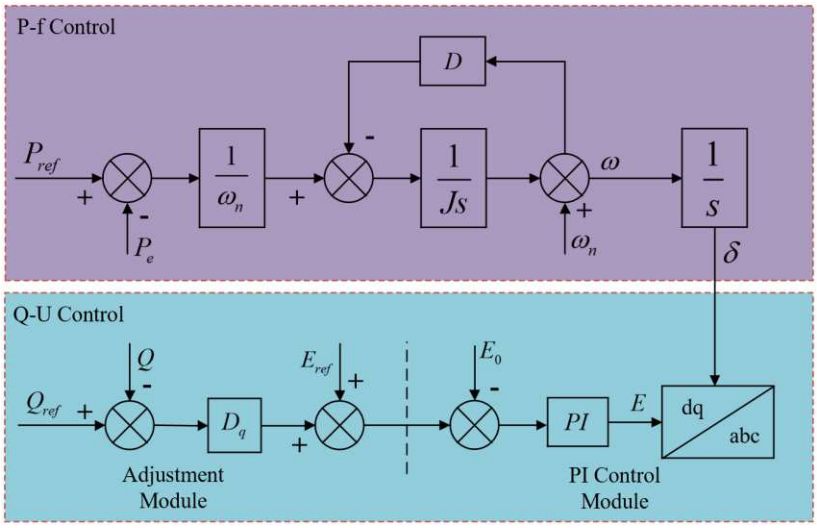

Fig. 3 VSG control block diagram.

Dynamic Characteristic Analysis of Virtual Inertia and Damping

To intuitively evaluate the impact of virtual inertia (J) and the damping coefficient (D) on the microgrid's dynamic behavior, time-domain simulations are conducted under varying parameter configurations. The corresponding active power and system frequency trajectories are presented in Fig. 4 and Fig. 5.

An examination of the transient response in Fig. 4(b) reveals that scaling up the virtual inertia from 0.1 to 0.5 significantly flattens the rate of change of frequency (RoCoF) and restricts the peak transient frequency deviation during load or reference power steps. However, this enhanced inertial support introduces an inevitable drawback: as observed in Fig. 4(a), a larger J substantially prolongs the power oscillation period, delaying the system's return to a steady state.

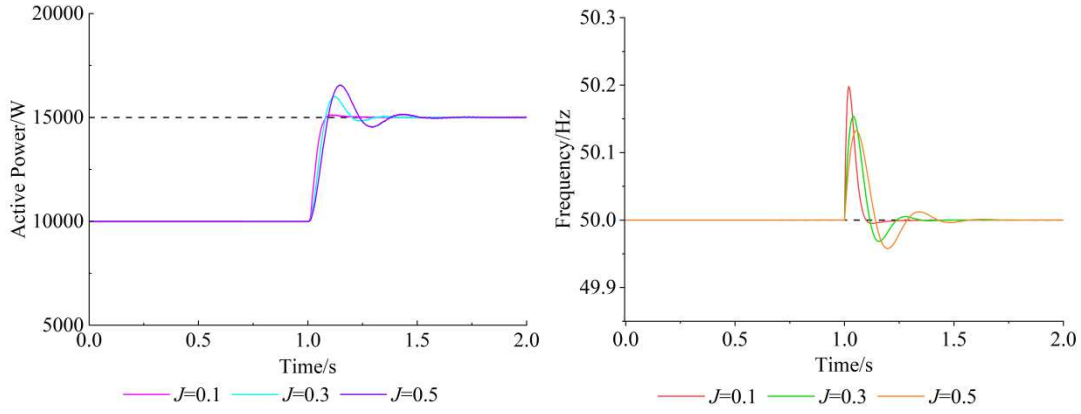

(a) (b)

Fig. 4 Dynamic responses of PV storage VSG system under varied virtual inertia J. (a) Active power output. (b) System frequency.

Conversely, Fig. 5 elucidates the regulatory role of the damping coefficient. While keeping J constant, an increment in D (from 5 to 15) acts as a powerful oscillation suppressor. The frequency and active power curves clearly indicate that higher damping accelerates the attenuation of transient fluctuations and minimizes overshoot.

These graphical results empirically expose an inherent contradiction in conventional VSG implementations. Relying on fixed parameters forces a structural compromise: prioritizing transient frequency stability (via large J and D) necessitates aggressive instantaneous power injection from the primary energy source. Under conditions where the battery operates at a low state-of-charge (SOC), commanding such massive transient discharge currents can severely degrade battery health or trigger irreversible hardware protection. Consequently, a fixed-parameter scheme is fundamentally inadequate for complex microgrid operations, establishing an urgent need for a dynamic, SOC-constrained adaptive regulation mechanism.

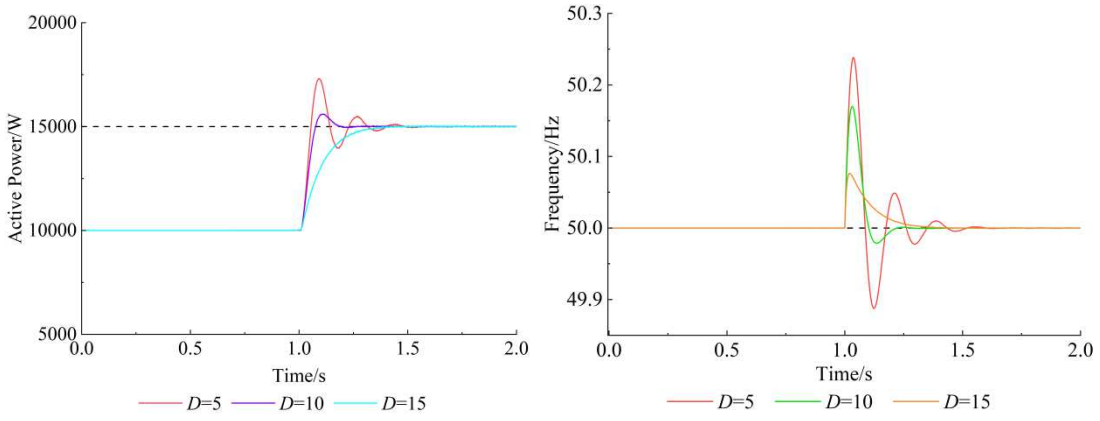

(a) (b)

Fig. 5 Dynamic responses of PV storage VSG system under varied damping D. (a) Active power output. (b) System frequency.

VSG has the characteristics of flexible adjustment of virtual inertia and virtual damping. Based on this feature, a traditional VSG adaptive control strategy was proposed. This strategy adjusts the virtual inertia and virtual damping in real time according to the frequency variation and frequency variation rate of the system, aiming to accelerate the frequency response speed and reduce the frequency overshoot. The output of photovoltaic power generation is fluctuating, so the power supply side often has energy storage devices to smooth out power fluctuations. However, as the frequency response speed increases, the overcharging and overdischarging problems of the energy storage equipment will damage the battery health and reduce its service life. Therefore, the relationship between the SOC of the energy storage battery and the virtual inertia of VSG is analyzed in the photovoltaic energy storage system, and an improved VSG parameter adaptive control strategy considering the SOC constraint of the energy storage equipment is proposed. This strategy takes into account the restrictions of the energy storage SOC on J and D, accelerates the frequency response speed, improves the frequency stability of the system, and effectively reduces the risk of overcharging or overdischarging of the energy storage equipment, which is conducive to battery health management.

Traditional VSG Parameter Adaptive Control Strategy

To elucidate the dynamic requirements of virtual parameters, Fig. 6 illustrates the electromechanical transient trajectories of a synchronous generator encountering an active power step disturbance. The entire oscillation process, progressing from the initial equilibrium to a new steady state, can be distinctively mapped into four transient stages based on the signs of the frequency deviation ($\Delta\omega$) and the rate of change of frequency ($d\omega/dt$).

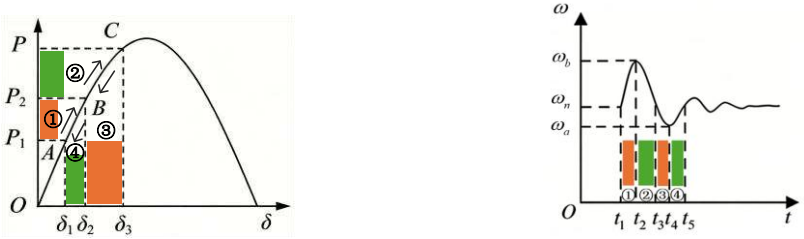

(a) (b)

Fig. 6 Power angle characteristic and angular frequency oscillation curve of synchronous generator. (a) Power angle curve. (b) Angular frequency curve.

According to Eq. (1), the transient frequency dynamics and the power coupling relationships can be explicitly expressed as:

$$\Delta\omega = \frac{T_m - T_e - J\frac{d\omega}{dt}}{D} \tag{2}$$

$$\frac{d\omega}{dt} = \frac{T_m - T_e - T_d}{J} \tag{3}$$

By analyzing the phase portraits of the frequency oscillations, a traditional coordinated adaptive strategy can be derived to mitigate transient instability, as summarized in Table 1[19]. The fundamental regulating philosophy of this conventional approach focuses on dynamically alternating the dominance of virtual inertia (J) and damping (D) across different oscillation stages.

Specifically, during the initial transient onset (Stages ① and ③), where $d\omega/dt$ exhibits substantial magnitude, the system urgently requires enhanced inertial support to restrict the rate of frequency excursion. Consequently, the controller aggressively increases J while keeping D at a moderate baseline to avoid sluggish initial responses. Conversely, as the system crosses the frequency nadir or peak and enters the recovery phases (Stages ② and ④), the primary control objective shifts from resisting sudden changes to rapidly dissipating the transient oscillation energy. In these phases, a larger D is strictly enforced to accelerate attenuation, alongside a deliberately reduced J that facilitates a swifter restoration to the nominal frequency.

Table 1. Regulation laws of *J* and *D*.

Stage	$d\omega/dt$	$\Delta\omega$	Trend of J	Trend of D	Trend of $\Delta\omega$
①	>0	>0	Increase	Maintain	Increase
②	<0	>0	Decrease	Increase	Decrease
③	<0	<0	Increase	Maintain	Increase
④	>0	<0	Decrease	Increase	Decrease

To quantitatively realize the piecewise adaptive rules in Table 1, the ideal unconstrained virtual inertia J_{ideal} and damping D_{ideal} are continuously formulated based on real-time frequency excursions ($\Delta\omega$) and Rate of Change of Frequency ($d\omega/dt$):

$$J_{ideal} = \begin{cases} J_0 & |d\omega/dt| \le T_J \\ J_0 + \mu_J|\omega-\omega_n| & \Delta\omega(d\omega/dt)<0 \cap |d\omega/dt| \ge T_J \\ J_0 + \mu_J|\omega-\omega_n| + k_J\left|\frac{d\omega}{dt}\right| & \Delta\omega(d\omega/dt)\ge 0 \cap |d\omega/dt| \ge T_J \end{cases} \tag{4}$$

$$D_{ideal} = \begin{cases} D_0 & \Delta\omega \le T_{D0} \\ D_0 + \mu_D|\omega-\omega_n| & \Delta\omega > T_{D0} \cap d\omega/dt \le T_D \\ D_0 + k_D\left(\frac{d\omega}{dt}\right)^2 + \mu_D|\omega-\omega_n| & \Delta\omega > T_{D0} \cap d\omega/dt > T_D \end{cases} \quad (5)$$

In Eq. (4) and (5), $J_0 = 0.2$ kg • m^2 and $D_0 = 10$ N • m • s/rad denote the baseline virtual inertia and damping coefficients, respectively. The proportional gains (μ_J, μ_D) and differential gains (k_J, k_D) dictate the sensitivity of parameter adaptation with respect to frequency excursions ($|\Delta\omega|$) and RoCoF ($|d\omega/dt|$). The threshold parameters (T_J, T_{D0}, T_D) establish insensitivity zones against grid measurement noise. Following the heuristic tuning procedure established in our previous work[23], these adaptation gains are systematically selected within the small-signal stability boundaries via time-domain optimization to balance frequency tracking and dynamic damping before being dynamically scaled by the proposed BESS SOC constraints.

While the aforementioned unconstrained adaptive rules (J_{ideal} and D_{ideal}) effectively optimize the electromechanical transient profile from the AC grid's perspective, they expose a critical vulnerability regarding the physical constraints of the primary energy source. Dictating massive transient power injections through large virtual inertia completely ignores the actual operational boundaries of the DC-link energy storage. If the battery operates under a critically low State-of-Charge (SOC), compelling it to output severe instantaneous surge currents to satisfy the traditional adaptive J demands will inevitably accelerate battery degradation or trigger irreversible undervoltage protection. Thus, relying solely on this conventional mechanism is inadequate, necessitating the introduction of a more robust, SOC-aware constrained adaptive strategy.

SOC-aware adaptive strategy with deadband and smoothing filter

While the conventional adaptive parameters mathematically optimize the AC-side frequency response, they implicitly assume an infinite energy buffering capacity from the DC-link source. In reality, the dynamic adjustment of virtual inertia directly dictates the instantaneous transient power drawn from the battery. This physical coupling is quantitatively illustrated in Fig. 7, which depicts the trajectories of the battery output power (P_{bat}) under varying inertia configurations during a step active power disturbance at $t = 1.0$ s.

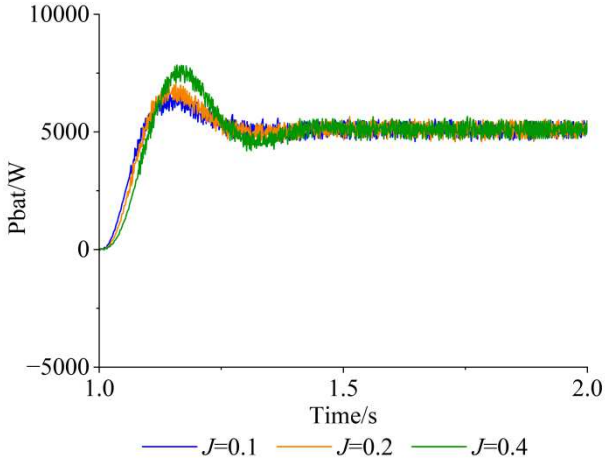

Fig. 7 Changes in Energy Storage Output Power under Different J.

It is evident that a larger virtual inertia ($J = 0.4$) induces a significantly higher transient power overshoot, pushing the peak demand well above the steady-state requirement. This heightened transient phase forces the energy storage system to sustain severe electrical stress. If the battery operates near its physical safety margins (e.g., a critically low SOC), compelling it to execute these massive inertial support commands will severely accelerate degradation or trigger undervoltage hardware protections. Consequently, the ideal virtual parameters must be dynamically penalized based on real-time SOC constraints.

To safeguard the energy storage hardware, an SOC-aware penalty factor, denoted as $\rho_{soc} \in [\rho_{min}, 1]$, is introduced to constrain the ideal inertia and damping directives. The regulation mechanism is bifurcated into discharging and charging scenarios, contingent upon the directional requirement of the grid power exchange. During periods of sudden increases in active power demand ($\Delta\omega > 0$), the battery is required to discharge. The corresponding penalty factor is formulated as:

$$\rho_{soc} = \begin{cases} 1 & SOC_{bat} \geq SOC_L \\ \rho_{min} + (1 - \rho_{min}) \left(\dfrac{SOC_{bat} - SOC_{min}}{SOC_L - SOC_{min}} \right)^k & SOC_{min} < SOC_{bat} < SOC_L \\ \rho_{min} & SOC_{bat} \leq SOC_{min} \end{cases} \tag{6}$$

Where SOC_L and SOC_{min} represent the conservative lower warning threshold and the absolute minimum discharge limit, respectively. The coefficient ρ_{min} is the predefined minimum attenuation ratio, ensuring that the VSG does not entirely lose its inertial characteristics. The exponent k (set to 2 in this study) determines the non-linear decay rate of the penalty function. When the battery level is ample ($SOC_{bat} \geqslant SOC_L$), ρ_{soc} equals 1, allowing the conventional adaptive strategy to fully dictate the dynamics. However, as the SOC drops into the critical zone, the penalty factor non-linearly decays, forcing the VSG to gracefully moderate its transient frequency-supporting output, thereby significantly alleviating transient current stresses and mitigating the risks of deep battery discharge[31].

Conversely, during an event ($\Delta\omega < 0$) requiring the battery to absorb surplus power, a symmetrical charging constraint is activated to prevent overcharging:

$$\rho_{soc} = \begin{cases} 1 & SOC_{bat} \leq SOC_H \\ \rho_{min} + (1 - \rho_{min}) \left(\dfrac{SOC_{max} - SOC_{bat}}{SOC_{max} - SOC_H} \right)^k & SOC_H < SOC_{bat} < SOC_{max} \\ \rho_{min} & SOC_{bat} \geq SOC_{max} \end{cases} \tag{7}$$

Where SOC_H and SOC_{max} denote the upper warning threshold and the absolute maximum charge limit, respectively.

Although the piecewise functions theoretically constrain the power flow, directly multiplying ρ_{soc} with the ideal VSG parameters in practical digital controllers introduces operational hazards. Minor steady-state numerical noise or slight frequency deviations can frequently trigger the penalty logic, resulting in high-frequency chattering of the virtual parameters. Furthermore, instantaneous transitions across the SOC boundary thresholds can induce step changes in J and D, provoking secondary power oscillations.

To overcome these engineering bottlenecks, a frequency deviation deadband ($\omega_{deadband}$) and a discrete first-order low-pass filter are seamlessly integrated into the regulation loop. The penalty logic is exclusively activated when the absolute frequency variation exceeds $\omega_{deadband}$; otherwise, the system operates in a steady-state quiet zone with no parameter attenuation ($\rho_{soc} = 1$). Furthermore, the raw penalty factor is processed through a digital smoothing filter before execution:

$$\rho_{soc_filtered} = \alpha \cdot \rho_{soc} + (1 - \alpha) \cdot \rho_{soc_prev} \tag{8}$$

Where $\alpha \in (0, 1)$ is the discrete filtering coefficient, and ρ_{soc_prev} is the historical value from the previous control cycle. Ultimately, the final coordinated parameters dispatched to the VSG inner loop are expressed as:

$$\begin{cases} J_{actual} = J_{ideal} \cdot \rho_{soc_filtered} \\ D_{actual} = D_{ideal} / \rho_{soc_filtered} \end{cases} \tag{9}$$

By implementing this comprehensive architecture, the proposed strategy dynamically negotiates the trade-off between grid frequency stability and electrochemical energy buffer preservation. It should be noted that the proposed SOC-aware penalty factor operates at the primary converter control layer as an active stress-mitigation mechanism; physical overdischarge cutoff and strict cell-level threshold enforcement remain governed by the dedicated Battery Management System (BMS) hardware protection.

Tuning of Base Parameters and Control Constraints

The base inertia J_0 and damping coefficient D_0 define the foundational dynamic response of the VSG. To ensure satisfactory steady-state frequency regulation within a ±0.5 Hz allowable deviation under a nominal 10 kW disturbance, the baseline damping coefficient is constrained by the maximum torque boundaries and configured as $D_0 = 10$ N·m·s/rad. Similarly, to restrict the rate of change of frequency (RoCoF) without excessively prolonging the settling time (t_s), the nominal virtual inertia is selected as $J_0 = 0.2$ kg·m^2, complying with the classical inertia time constant range ($H \in$[2s, 9s]).

For the proposed SOC-aware constraint mechanism, the selection of the lower bound attenuation factor ρ_{min}, deadband threshold $\omega_{deadband}$, and smoothing coefficient requires a deliberate engineering balance:

1. Minimum Attenuation Limit (ρ_{min}): Configuring $\rho_{min} = 0.1$, prevents the virtual inertia from vanishing entirely ($J_{actual} > 0$). Dropping J to zero would collapse the synchronous generator emulation, transforming the converter into a memoryless static current source and risking phase-lock instability. Setting $\rho_{min} = 0.1$ retains a minimal inertial anchor while shedding 90% of the battery transient current burden.

2. Deadband Threshold ($\omega_{deadband}$): In practical digital controllers, grid frequency measurements inherently suffer from high-frequency noise and quantization errors. Setting $\omega_{deadband} = 0.03$ rad/s (approx. 0.005Hz) creates an insensitivity buffer, ensuring that the SOC penalty logic is triggered only by genuine power step disturbances rather than ambient measurement noise.

3. Smoothing Filter Coefficient (α): The discrete filtering factor α governs the equivalent time constant of parameter updates ($\tau_f = T_s / \alpha$, where T_s is the control sampling period). With $T_s = 5\mu s$, configuring $\alpha = 0.01$ establishes a smooth parameter transition trajectory that filters out boundary-crossing step chattering without inducing noticeable control phase delays relative to the electromechanical oscillation period.

Small-Signal Stability Proof under SOC Attenuation

A critical criterion for the proposed control framework is ensuring that dynamic reductions in virtual parameters do not jeopardize system stability. Based on the fundamental active power-frequency (P-f) regulation loop established in the previous text and its classical small-signal equivalent model, the dominant dynamic behavior of the VSG active power control is governed by a typical second-order characteristic equation[10]:

$$s^2 + \frac{D_{actual}}{J_{actual}} s + \frac{EU}{J_{actual}\omega_n X_s} = 0 \tag{10}$$

During a low-SOC event where the penalty factor is active ($\rho_{soc_filtered} \in [\rho_{min}, 1]$), the actual coordinated parameters are scaled as $J_{actual} = \rho_{soc_filtered} \cdot J_{ideal}$ and $D_{actual} = \rho_{soc_filtered} / D_{ideal}$. Substituting these scaled variables into the characteristic second-order parameters yields the effective natural oscillation frequency ($\omega_{n,eff}$) and damping ratio (ζ_{eff}):

$$\omega_{n,eff} = \frac{1}{\sqrt{\rho_{soc_filtered}}} \cdot \omega_{n,ideal} \tag{11}$$

$$\zeta_{eff} = \frac{D_{actual}}{2}\sqrt{\frac{\omega_n X_s}{J_{actual} EU}} = \frac{1}{\rho_{soc_filtered}^{1.5}} \cdot \zeta_{ideal} \tag{12}$$

As revealed by Eq. (12), because the penalty factor satisfies $\rho_{soc_filtered} \in [\rho_{min}, 1]$, the effective damping ratio ($\zeta_{eff} = \rho_{soc_filtered}^{-1.5} \cdot \zeta_{ideal}$) actually increases dynamically during the low-SOC penalty interval. This amplified equivalent damping effectively shifts the closed-loop system into an overdamped transient state, explaining why transient power overshoots are completely eradicated. Accordingly, based on the characteristic polynomial in Eq. (10), the dominant closed-loop eigenvalues $s_{1,2}$ across the adaptation process are explicitly derived as:

$$s_{1,2} = -\frac{D_{ideal}}{2\rho_{soc_filtered}^2 J_{ideal}} \pm j\omega_{n,eff}\sqrt{1 - \zeta_{eff}^2} \tag{13}$$

Since the baseline control parameters J_{ideal} and D_{ideal} are strictly positive constants, and the SOC penalty factor $\rho_{soc_filtered}$ is bounded within the strictly positive range of $[0.1, 1]$, the real part of the characteristic roots ($\mathrm{Re}(s_{1,2}) = -D_{ideal}/2\rho_{soc_filtered}^2 J_{ideal}$) remains strictly negative. Consequently, all dominant system eigenvalues are analytically confined to the Left-Half Plane (LHP), analytically confirming closed-loop small-signal stability across the nominal parameter adaptation trajectory.

References

[1] Choudhury, S. A comprehensive review on issues, investigations, control and protection trends, technical challenges and future directions for microgrid technology. *Int. Trans. Electr. Energy Syst.* **30**, e12446. https://doi.org/10.1002/2050-7038.12446 (2020).

[2] Saeed, M. H., Fangzong, W., Kalwar, B. A. & Iqbal, S. A review on microgrids' challenges & perspectives. *IEEE Access* **9**, 166502–166517. https://doi.org/10.1109/ACCESS.2021.3135800 (2021).

[3] Shahzad, S. et al. Possibilities, challenges, and future opportunities of microgrids: A review. *Sustainability* **15**, 6366. https://doi.org/10.3390/su15086366 (2023).

[4] Arévalo, P. et al. Smart microgrid management and optimization: A systematic review towards the proposal of smart management models. *Algorithms* **18**, 429. https://doi.org/10.3390/a18070429 (2025).

[5] Wang, L. et al. Variable parameter VSG control based on adaptive exponential function. *J. Electr. Power Sci. Technol.* **38**, 124 – 131. https://doi.org/10.19781/j.issn.1673-9140.2023.03.013 (2023).

[6] Heidary, J., Gheisarnejad, M., Rastegar, H. & Khooban, M. H. Survey on microgrids frequency regulation: Modeling and control systems. *Electr. Power Syst. Res.* **213**, 108719. https://doi.org/10.1016/j.epsr.2022.108719 (2022).

[7] Luckose, V., Khan, A. R., Razak, N. F. H. A. & Subramani, G. A comprehensive analysis of dissolved gases in oil to monitor suspicious faults of distribution transformers in solar farm. *J. Eng. Technol. Adv.* **10**, 82 – 105. https://doi.org/10.35934/segi.v10i2.161 (2025).

[8] Wang, J., Ramli, N. & Aziz, N. H. A. Pre synchronization control strategy of virtual synchronous generator (VSG) in micro-grid. *IEEE Access* **11**, 139004 – 139016. https://doi.org/10.1109/ACCESS.2023.3338309 (2023).

[9] Pian, H. et al. An adaptive control strategy for a virtual synchronous generator based on exponential inertia and nonlinear damping. *Energies* **18**, 3822. https://doi.org/10.3390/en18143822 (2025).

[10] Altawallbeh, A., Alassi, A., Meskin, N., Al-Hitmi, M. A. & Massoud, A. M. Small-signal stability analysis and parameters optimization of virtual synchronous generator for low-inertia power system. *IEEE Access* **13**, 107227 – 107243. https://doi.org/10.1109/ACCESS.2025.3538412 (2025).

[11] Long, B., Liao, Y., Chong, K. T., Rodríguez, J. & Guerrero, J. M. MPC-controlled virtual synchronous generator to enhance frequency and voltage dynamic performance in islanded microgrids. *IEEE Trans. Smart Grid* **12**, 953 – 964. https://doi.org/10.1109/TSG.2020.3019808 (2020).

[12] Zhang, W., Cantarellas, A. M., Rocabert, J., Luna, A. & Rodriguez, P. Synchronous power controller with flexible droop characteristics for renewable power generation systems. *IEEE Trans. Sustain. Energy* **7**, 1572 – 1582. https://doi.org/10.1109/TSTE.2016.2541178 (2016).

[13] Tang, W. et al. An adaptive inertia and damping control strategy for virtual synchronous generators to enhance transient performance. *Energies* **19**, 204. https://doi.org/10.3390/en19010204 (2025).

[14] Jafari, M., Gharehpetian, G. B. & Anvari-Moghaddam, A. Adaptive fuzzy logic-based coordinated tuning of distributed virtual synchronous generators parameters for frequency oscillation suppression in islanded microgrids. *Electr. Power Syst. Res.* **254**, 112656. https://doi.org/10.1016/j.epsr.2026.112656 (2026).

[15] Awda, Y. & Alowaifeer, M. Adaptive optimization of virtual synchronous generator based on fuzzy logic control and differential evolution. *Ain Shams Eng. J.* **15**, 102606. https://doi.org/10.1016/j.asej.2023.102606 (2024).

[16] Zhou, A., Liu, X., Wu, D. & Ge, J. A dynamic particle swarm optimization approach for identifying control parameters of virtual synchronous generators. In *Proc. 2025 4th International Conference on Energy and Electrical Power Systems (ICEEPS)* 829 – 833. https://doi.org/10.1109/ICEEPS64478.2025.10984852 (IEEE, 2025).

[17] Assogna, R., Ciabattoni, L. & Comodi, G. PSO-based supervisory adaptive controller for BESS-VSG frequency regulation under high PV penetration. *Energies* **18**, 5401. https://doi.org/10.3390/en18205401 (2025).

[18] Xiao, Q. et al. Adaptive virtual inertia emulation and control scheme of cascaded multilevel converters to maximize its frequency support ability. *IEEE Trans. Ind. Electron.* https://doi.org/10.1109/TIE.2025.3530291 (2025).

[19] Alipoor, J., Miura, Y. & Ise, T. Power system stabilization using virtual synchronous generator with alternating moment of inertia. *IEEE J. Emerg. Sel. Topics Power Electron.* **3**, 451 – 458. https://doi.org/10.1109/JESTPE.2014.2362530 (2014).

[20] Awal, M. & Husain, I. Transient stability assessment for current-constrained and current-unconstrained fault ride through in virtual oscillator-controlled converters. *IEEE J. Emerg. Sel. Topics Power Electron.* **9**, 6935 – 6946. https://doi.org/10.1109/JESTPE.2021.3060662 (2021).

[21] Karimi, A., Jafarian, Y., Mirzaee, R. & Bevrani, H. Frequency response improvement in microgrids: A fuzzy-based virtual synchronous generator approach. *Int. J. Ind. Electron. Control Optim.* **3**, 147–158. https://doi.org/10.22111/ieco.2019.29879.1174 (2020).

[22] Wang, L. et al. Adaptive inertia and damping coordination (AIDC) control for grid-forming VSG to improve transient stability. *Electronics* **12**, 2060. https://doi.org/10.3390/electronics12092060 (2023).

[23] Li, H., Ramli, N., Wang, J., Chong, H. S. & Zhang, X. Coordinated adaptive VSG control strategy based on virtual inertia and damping. *IEEE Access* **14**，63991-64001. https://doi.org/10.1109/ACCESS.2026.3686834 (2026).

[24] Bandla, K. C., Gururaj, M. & Padhy, N. P. Decentralized and coordinated virtual synchronous generator control for hybrid AC-DC microgrids. In *Proc. 2020 IEEE International Conference on Power Electronics, Smart Grid and Renewable Energy (PESGRE)* 1 – 6. https://doi.org/10.1109/PESGRE49394.2020.9329712 (IEEE, 2020).

[25] Zeng, Z., Gajare, P. M., Divan, D. & Saeedifard, M. Impact of DC voltage reference on subsynchronous dynamics in grid-forming inverters. *IEEE Trans. Power Electron.* **40**, 8934 – 8938. https://doi.org/10.1109/TPEL.2025.3533814 (2025).

[26] Luo, C., Liu, T., Wang, X. & Ma, X. Design-oriented analysis of DC-link voltage control for transient stability of grid-forming inverters. *IEEE Trans. Ind. Electron.* **71**, 3698 – 3707. https://doi.org/10.1109/TIE.2023.3270519 (2023).

[27] Ray, I. & Tolbert, L. M. Grid-forming inverter control design for PV sources considering DC-link dynamics. *IET Renew. Power Gener.* **19**, e12454. https://doi.org/10.1049/rpg2.12454 (2025).

[28] Xing, W. et al. An adaptive virtual inertia control strategy for distributed battery energy storage system in microgrids. *Energy* **233**, 121155. https://doi.org/10.1016/j.energy.2021.121155 (2021).

[29] Zhang, X. et al. Fuzzy adaptive virtual inertia control of energy storage systems considering SOC constraints. *Energy Rep.* **9**, 2431 – 2439. https://doi.org/10.1016/j.egyr.2023.01.077 (2023).

[30] Zhou, L., Jin, X., Chun, E., Wang, Z. & Liu, J. Thermal behavior and failure mechanisms of lithium-ion battery under high discharging rate. *Appl. Therm. Eng.* **278**, 127043. https://doi.org/10.1016/j.applthermaleng.2025.127043 (2025).

[31] Qian, L. et al. Revealing the impact of high current overcharge/overdischarge on the thermal safety of degraded Li-ion batteries. *Int. J. Energy Res.* **2023**, 8571535. https://doi.org/10.1155/2023/8571535 (2023).

[32] You, F. et al. A state-of-charge-based flexible synthetic inertial control strategy of battery energy storage systems. *Front. Energy Res.* **10**, 908361. https://doi.org/10.3389/fenrg.2022.908361 (2022).

[33] Karaki, A., Sharida, A., Bayhan, S. & Abu-Rub, H. A parameter-adaptive predictive control strategy for grid-connected inverters with different filter topologies. *IEEE Trans. Ind. Electron.* **73**, 706–717. https://doi.org/10.1109/TIE.2025.3591708 (2026).

[34] Xu, J., Qian, H., Hu, Y., Bian, S. & Xie, S. Overview of SOGI-based single-phase phase-locked loops for grid synchronization under complex grid conditions. *IEEE Access* **9**, 39275 – 39291. https://doi.org/10.1109/ACCESS.2021.3063515 (2021).

[35] Ji, Y. et al. Exponential synergistic adaptive control for PV – storage grid-forming inverters to eliminate overdamped hysteresis in weak grids. *Electronics* **15**, 1273. https://doi.org/10.3390/electronics15061273 (2026).

[36] Xia, Y. et al. A virtual synchronous generator control strategy based on transient damping compensation and virtual inertia adaptation. *Appl. Sci.* **15**, 728. https://doi.org/10.3390/app15020728 (2025).

[37] Abadi, S. A. G. K., Habibi, S. I., Khalili, T. & Bidram, A. A model predictive control strategy for performance improvement of hybrid energy storage systems in DC microgrids. *IEEE Access* **10**, 25400 – 25421. https://doi.org/10.1109/ACCESS.2022.3155824 (2022).

[38] Zhong, Q.-C. & Weiss, G. Synchronverters: Inverters that mimic synchronous generators. *IEEE Trans. Ind. Electron.* **58**, 1259 – 1267. https://doi.org/10.1109/TIE.2010.2048839 (2011).

Funding

This work was supported by the Project of Science and Technology Research Program of Chongqing Municipal Education Commission, China. (Project No. KJQN202605409, Project Name “Research on VSG Coordinated Adaptive Control Strategy Based on Virtual Inertia and Damping”).

Author contributions

Hui Li: Writing–original draft, Methodology, Conceptualization, Software, Formal analysis;

Nurulazlina Ramli: Writing – review & editing, Supervision, Project administration, Resources;

Jianfeng Wang: Validation, Investigation, Data curation.

Data availability

The data presented in this study are available upon request from the corresponding author.

Competing Interests Statement

The authors declare no competing interests.